Project 005 Noise Emission and Propagation Modeling

Pennsylvania State University
Purdue University

Project Lead Investigator

Victor W. Sparrow
Director and Professor of Acoustics
Graduate Program in Acoustics
Penn State
201 Applied Science Bldg.
University Park, PA 16802
+1 (814) 865-6364
vws1@psu.edu

University Participants

Pennsylvania State University

- P.I.: Victor W. Sparrow, Professor of Acoustics
- FAA Award Number: 13-C-AJFE-PSU, amendments 005, 015, 029.
- Period of Performance: August 18, 2014 to December 31, 2017.
- Task(s):
    1. Assess applicability of meteorological reanalysis models for possible use in FAA noise tools
    2. Assess measurement data sets for noise propagation model validation

Purdue University

- P.I.(s): Kai Ming Li, Professor of Mechanical Engineering
- FAA Award Number: 13-C-AJFE-PU, amendments 002, 007, 009, 016
- Period of Performance: June 1, 2014 to June 2017.
    3. Extend model for fast moving sources

Project Funding Level

FAA funding to Penn State in 2014-2015 was $132K and in 2015-2015 was $110K. FAA funding to Purdue in 2014-2015 and 2015-2016 was $80K and $90K, respectively.

In-kind cost sharing from Vancouver Airport Authority received in October 2016 was $294,500 to Penn State and $294,500 to Purdue. The point of contact for this cost sharing is Mark Cheng, mark_cheng@yvr.ca . Project support is in the form of aircraft noise and trajectory data, meteorology data, and consulting on those datasets.

Investigation Team

Penn State

Victor W. Sparrow (PI)
Graduate Research Assistant Rachel Romond (meteorological reanalysis data investigation)
Graduate Research Assistant Manasi Biwalkar (measurement data sets for model validation investigation)

Purdue

Kai Ming Li (PI)
Graduate Research Assistant Bao Tong (moving source investigation)
Graduate Research Assistant Yiming Wang (moving source investigation)

Project Overview

The FAA has been funding research efforts in developing enhanced noise emission and propagation capabilities to better support environmental impact studies at both local and national levels. The main emphasis in the near and mid-term is to increase the Research Readiness Level (RRL) of the capabilities so that they can be further matured for implementation into the FAA tools. Validation of the modeling capabilities has been the central focus of the project. Via recent US-EU research collaboration, the field measurement database (BANOERAC) is becoming available for model validation. This database contains acoustic time history of flight events from various types of commercial aircraft during cruise, climb and descent phases of the flight. In addition the DISCOVER/AQ and Vancouver Airport Authority databases have already come on line for use in this and other FAA projects. These datasets make model validation possible. In addition the work will make existing models ready for simulating real weather conditions via proper treatment of the meteorological input parameters and to establish a common basis for comparing US and EU models.

Task 1 "Assess applicability of meteorological reanalysis models for possible use in FAA noise tools"

The Pennsylvania State University

Objective(s)

Determine if meteorological reanalysis datasets and corresponding input parameters are useful for aircraft noise propagation prediction and whether the same can be integrated into the AEDT noise analysis framework.

Research Approach [the first few subsections are repeated from the 2015 annual report, but included here as a convenience]

Introduction

AEDT's acoustic propagation algorithms currently assume a homogeneous and still propagation medium. This omits variable acoustic absorption and refraction (bending) of sound as the sound travels from the source to a receiver. Future versions of AEDT may be able to include refraction in sound propagation calculations by including the inhomogeneity of the medium. This would allow prediction of ranges of received sound level that would occur due to atmospheric effects. Currently available surface-based atmospheric models [Wilson, 2004] are not appropriate for analysis of flight operations because they rely on the theory of the atmospheric surface layer. The thickness of the surface layer changes throughout the day, but generally makes up the lowest ~300 m of the atmosphere. This constitutes less than 5% of the propagation path of sound emitted from a typical en-route aircraft and received on the ground.

To include the medium inhomogeneity at all altitudes relevant to en-route flight noise, accurate upper-air atmospheric data are required. The data source needs to have relatively high resolution, and needs to include all the atmospheric variables required to calculate an acoustic field. A perfectly realistic representation of the medium is not feasible in terms of both data availability and computational efficiency. It is necessary to find a compromise between a homogenous-atmosphere assumption and a perfect recreation of the atmosphere in all dimensions of time and space. The atmospheric data also need to be consistently collected and quality-controlled, represent an adequate spatial sampling of the propagation field, and be openly accessible. One type of data product that satisfies these criteria is meteorological reanalysis.

Reanalysis

Meteorological reanalysis is a process that incorporates measurements of the atmosphere into a long-term model of the earth's geologic-oceanic-atmospheric system to produce a 4-D representation of the atmosphere in space (latitude, longitude, and altitude) and time. In a global reanalysis, observations of the oceans and atmosphere are collected from around the world over an extended time span. These observations are fed into a physics-based model of the atmosphere in a detailed data assimilation process. Reanalysis incorporates many historical observations over an extended time period (years to decades) using a consistent oceanic-atmospheric model and data assimilation scheme. The model is run forward in time, and the calibration and settings/sensitivities of the model are periodically checked against the collected observations. The model is used to predict analysis states, which are best estimates of the state of the total atmosphere for a number of points in time over a distribution of spatial locations.

Currently, about a dozen state-of-the-art reanalysis products exist. They are conducted and maintained by different entities, and each use slightly different atmospheric models, data assimilation methods, analysis time spans, and spatial coverage and resolution. The appropriate choice of reanalysis product depends greatly on the intended use. We have investigated two of these current reanalysis products for possible use in representing the atmosphere in an aviation noise model. The two products are the NCDC/UCAR's Climate Forecast System Reanalysis (CFSR) [Saha, et al., 2010] and NASA's Modern-Era Retrospective Analysis for Research and Applications (MERRA) [NASA, 2012].

Both CFSR and MERRA provide analysis points every 6 hours from 1979 to the present, providing excellent temporal coverage and resolution. Both CFSR and MERRA provide global coverage at a geographic resolution better than 1 degree latitude by 1 degree longitude. Figure 5.1 shows the geographic coverage and resolution for CFSR over the continental United States. Both CFSR and MERRA have vertical coverage from the ground to well past the altitude required for analysis of en-route operations (up to approximately 48 km for CFSR and 65 km for MERRA). The vertical resolutions vary with altitude, but both products are similar, ranging from approximately 100 m (near the ground) to approximately 2 km (at an altitude of 20 km). In addition, both CFSR and MERRA contain the necessary data fields (ambient pressure, temperature, humidity, wind speed and wind direction) for calculation of the sound speed and acoustic absorption coefficient at altitude. CFSR contains additional data fields for temperature at the ground, humidity at 2 m, and wind speed at 10 m. CFSR was ultimately chosen for this proof-of-concept project because of these additional data fields and because of the accessibility of the data.

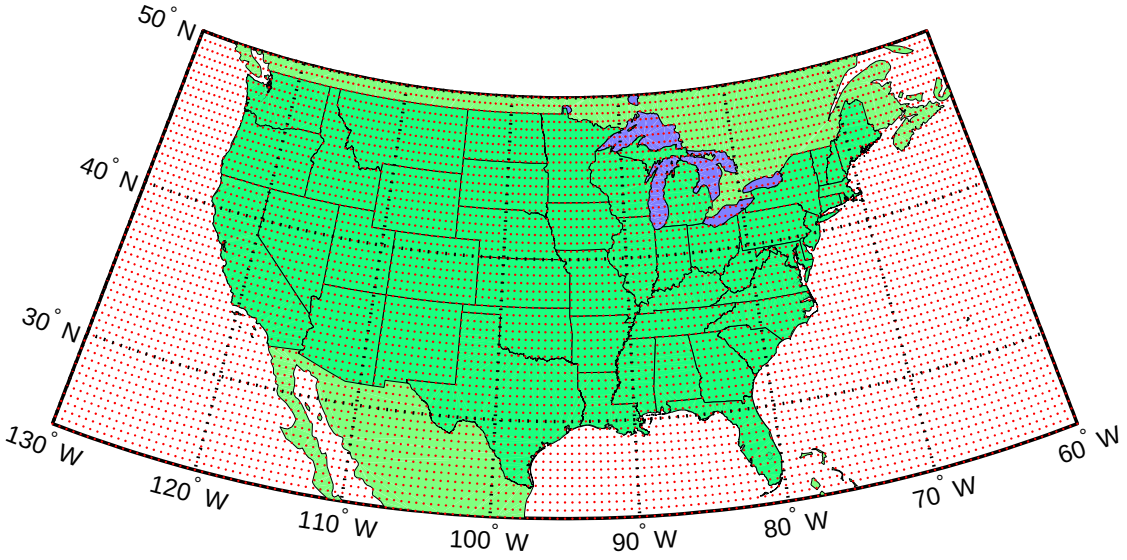

Fig. 5.1: Geographic distribution and resolution of CFSR analysis points (in red) over the continental United States. Figure by R. Romond.

Long-Term Metrics

Historical atmospheric data could be used to improve the prediction of long-term average noise metrics by including the effects of meteorological conditions on acoustical propagation. Based on methods by previous researchers [Salomons, van den Berg & Brackenhoff, 1994; Heimann & Salomons, 2004], the statistics of occurrence of meteorological conditions can be used to weight the sound level predictions for certain propagation conditions before they are averaged to find long-term average sound level predictions. To do this, long-term periodic meteorological measurements can be grouped into a number of classes, while the average meteorological conditions of each class *k* is used to calculate the received sound

levels L_k that would occur under each condition. If each class k happens w_k% of the time, the long-term average level L_{eq} is the weighted average of each class level L_k, or

$$L_{eq} = 10\log_{10}\sum_{k=1}^{N} w_k 10^{L_k/10}$$

Upper Atmosphere

As previously mentioned, methods exist to include measured atmospheric data in acoustic propagation calculations. However, the methods are based on measurements made at or near the ground, and they rely on Monin-Obukhov similarity theory of the atmospheric boundary layer theory to extrapolate the values higher into the atmosphere. These methods have been validated for ground-to-ground sound propagation, but Monin-Obukhov similarity theory is only valid for the lowest ~300 m of the atmosphere [Wyngaard, 2010]. The existing methods would only be appropriate for aircraft ground operations such as taxiing and run-ups. They would not be appropriate for analysis of air-to-ground propagation where an aircraft is at altitude.

It would be preferable to include the full atmospheric profiles extracted from the reanalysis data. This ensures that the entire propagation space is represented, and that few assumptions are made about the state of the atmosphere. If necessary, the extracted profiles can be simplified and/or parameterized. This might increase processing efficiency because only the parameterization coefficients would be carried through the calculation (rather than the full profiles). Two possible methods are curve-fitting and layering.

In curve-fitting, a vertical profile is represented by a mathematical function where altitude z is the independent variable and the temperature, wind speed/direction, humidity, or ambient pressure is the dependent profile. Functions currently being considered are linear, logarithmic, log-linear, and polynomial. In layering the atmospheric profiles are split up into layers. Each layer can be homogeneous, or linear/logarithmic/log-linear. A spline fit would combine curve-fitting and layering, but care must be taken to ensure that the function isn't over-determined and includes spatial variations ("wiggles") that don't exist in the raw data. In either case, it is important to accurately represent the value at the ground, the gradient, and both the location and value of any inflection points.

Approach Utilized

Figure 5.2 shows the method currently utilized, developed in 2015, for including CFSR atmospheric reanalysis data in an acoustic propagation model. The raw data is downloaded from UCAR and pre-processed to select relevant data fields for the geographic area under consideration. The raw data .grb files contain one year of 6-hourly global data per file. The pre-processing routine selects the analysis location (out of the available locations shown in Figure 5.1) closest to the airfield. Then, vertical profiles of temperature (T), wind speed and direction (u), humidity (h), and ambient pressure (P) are extracted. Either single-time profiles are chosen, or the profiles are averaged over the applicable time period. The resulting atmospheric profiles are then converted to profiles of acoustic variables. Temperature and wind speed/direction profiles are converted to a sound speed profile c(z). Temperature, humidity, and ambient pressure profiles are converted to an acoustic absorption coefficient profile $\alpha(z)$. Finally, the calculated sound speed and absorption profiles are entered into an acoustic ray tracing program, along with source parameters and receiver grid information. The ray tracing program then calculates the received noise contour at the ground, taking into account the atmospheric conditions originally extracted from the CFSR data set.

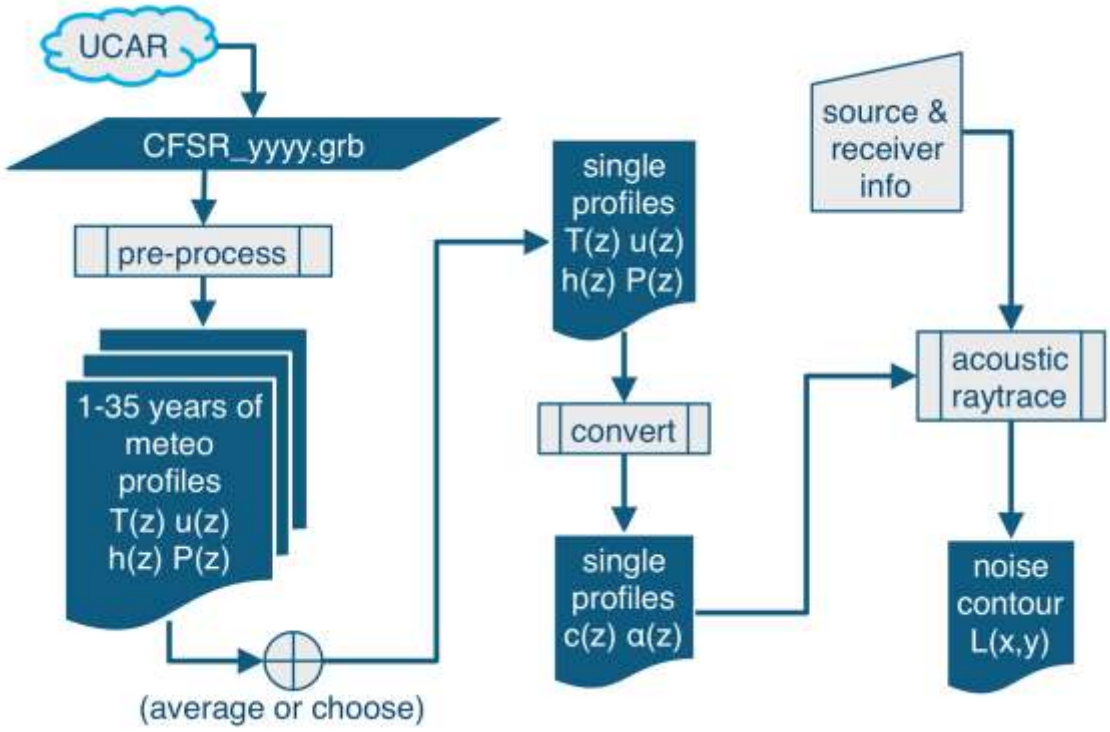

Fig. 5.2: Current method for integrating CFSR atmospheric data into a noise model. The meteorological profile parameters are temperature (T), wind speed and direction (u), humidity (h), ambient pressure (P). The profiles required by the acoustic ray tracing program are sound speed (c) and acoustic absorption coefficient (α). The independent variable for each profile is altitude (z).

Comparison of temperature profiles

It is instructive to compare the temperature profile representation between a typical CFSR (stars) output versus other continuous profiles in Figure 5.3. These stars represent an annual average temperature profile close to the Pittsburgh, PA airport in 2010. One can see that the homogeneous temperature profile (used by AEDT), is the black vertical line in the figure, and it is way off except at the ground. The linear fit to the CFSR is the straight blue line, and it fares somewhat better. The ICAO standard atmosphere profile in red, or the 7th order polynomial fit of the ICAO standard atmosphere, still don't match the CFSR data (stars) quite closely as the green 8th order polynomial fit to the CFSR data. One take away is that almost any representation is better than the homogeneous atmosphere representation.

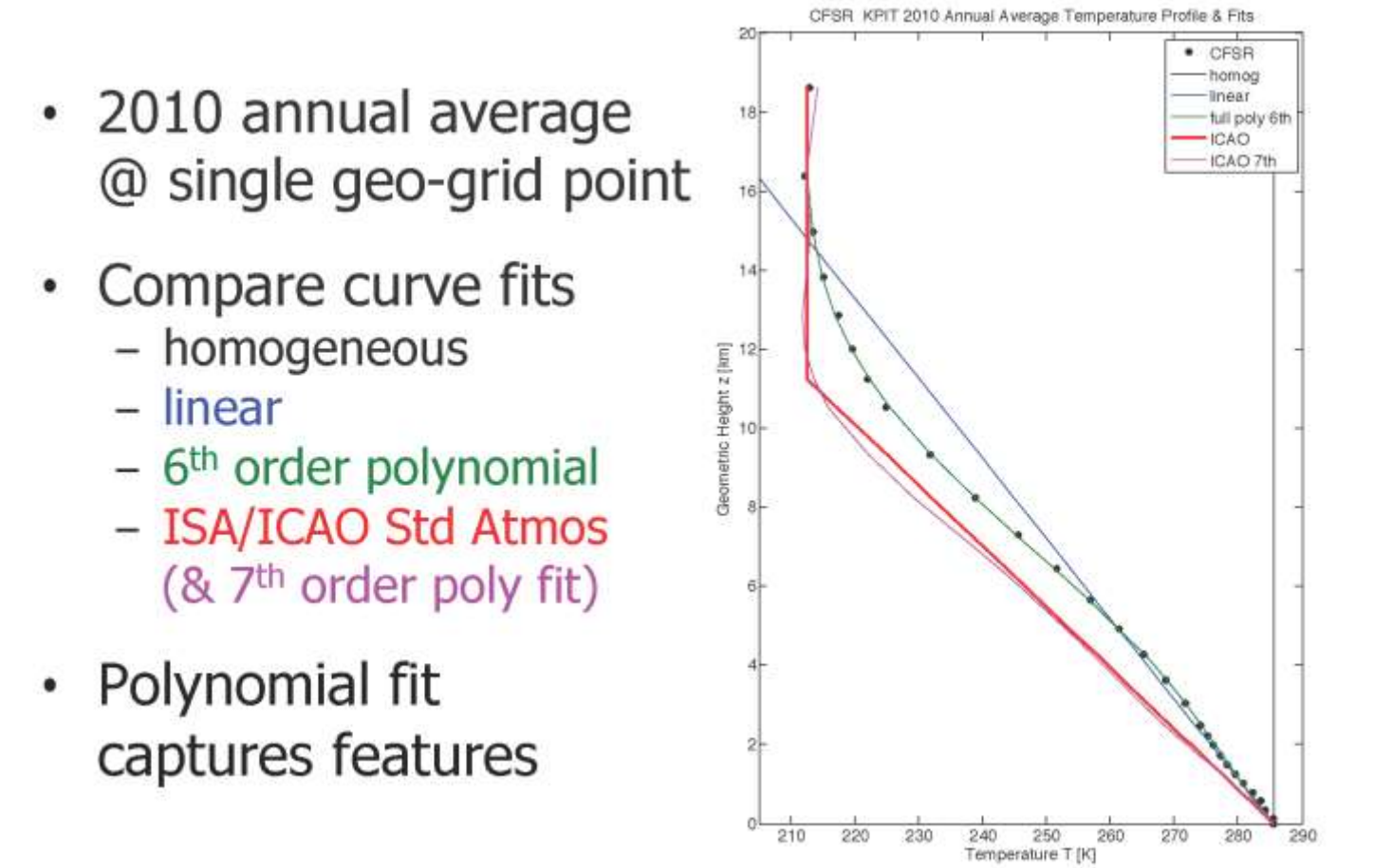

Fig. 5.3: Comparison of temperature profiles (lines) with CFSR data (stars). The homogeneous profile uses the surface values. The linear (blue) and 6th order polynomial (green) approximate the CFSR data. For comparison the ICAO standard atmosphere (red) and a 7th order polynomial fit to it (purple) are also shown.

Humidity profile representations

Knowing the humidity profile is essential for accurate atmospheric absorption calculations as a part of a noise propagation prediction, the project team investigated a number of ways to represent humidity in a consistent way in conjunction with the CFSR reanalysis paradigm. Figure 5.4 shows both a single CFSR profile (left) as well as an annual average (right) for relative humidity. It is clear that one must go to a very high order polynomial to follow the CFSR data, even for the annual average. The relative humidity profile is not a well behaved function.

Alternatively the project team looked at specific humidity, and it turns out to be much better behaved as a function of height. Referring to Figure 5.5, the same CFSR data is shown as in Fig 5.4, but now the specific humidity is much easier to represent with a low-order polynomial. Specific humidity is the number of grams of water vapor in 1 kilogram of air, and unlike relative humidity, specific humidity does not depend on temperature or pressure. One notices from Figure 5.5 that the specific humidity continuously decreases with height and looks somewhat like an exponential decay. Specific humidity simply seems to be better suited for inclusion in noise propagation studies. It should be noted that the SAE AIR 5534 atmospheric absorption implemented in AEDT employs the specific humidity.

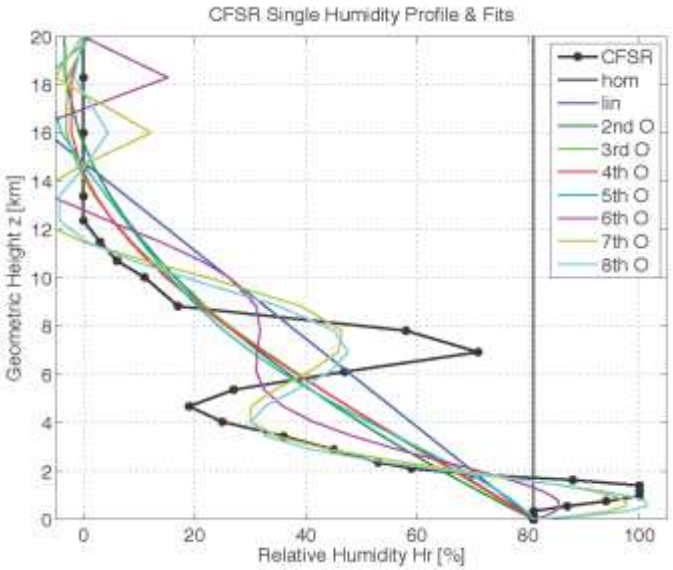

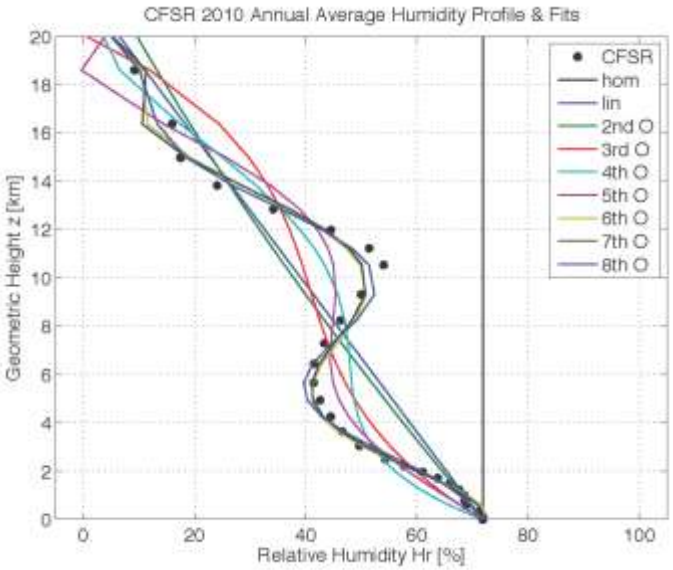

Fig. 5.4: Relative humidity data from CFSR with polynomial fits. Left: a single profile sample. Right: annual averaged profile.

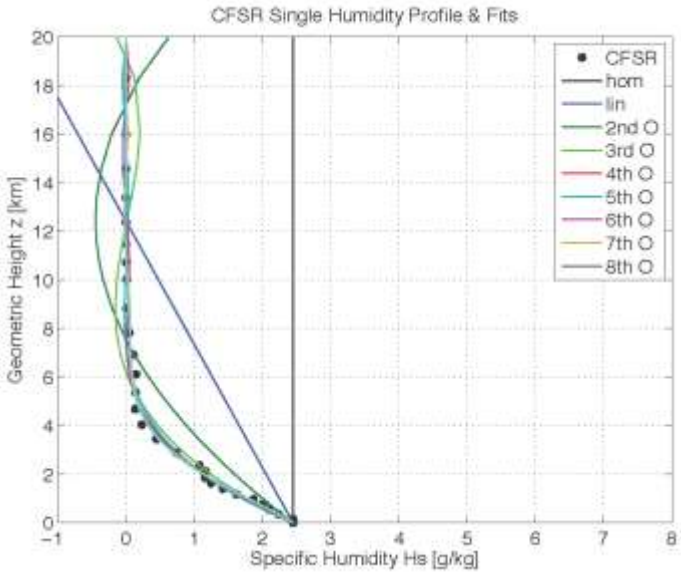

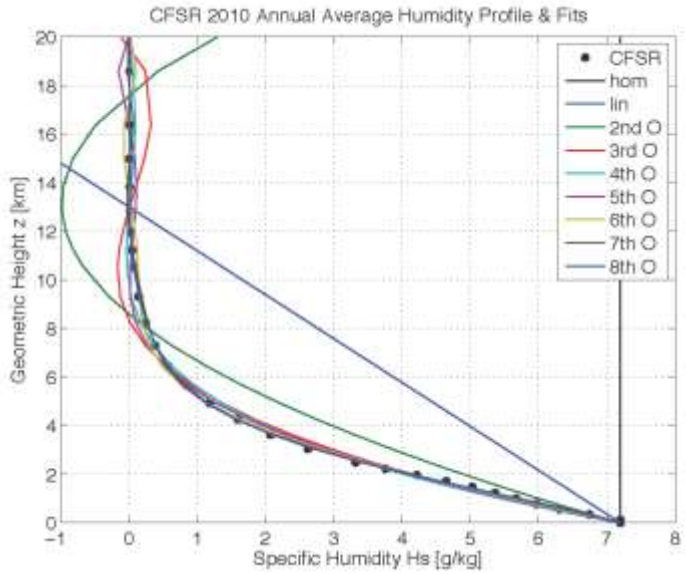

Fig. 5.5: Specific humidity data from CFSR with polynomial fits. Left: a single profile sample. Right: annual averaged profile. (Compare with Fig. 5.4.)

En-route sound pressure level differences on the ground due to different temperature and humidity profiles

At en-route altitudes, small differences in atmospheric absorption along the long propagation path make for large differences in sound levels on the ground. This is illustrated in Figure 5.6 showing sound pressure levels on the ground perpendicular to the direction of aircraft travel. The aircraft is flying steady at 275 m/s at a 10 km altitude. Four temperature profiles are shown with the different colors: black is the homogeneous atmosphere, blue is the linear fit to the CRFR temperatures, and green is the polynomial fit to the CFSR. The purple is the ICAO Standard Atmosphere temperature profile for comparison. The three line styles indicate the humidity used: dashed for dry air, thick/bold line for homogeneous humidity, and the thin line with dots is a polynomial fit to the CFSR humidity representation. One can quickly see that dry air (unrealistic) in the dashed lines leads to higher sound levels. The homogeneous temperature profile uses the surface value of temperature for all heights. It is seen that the homogenous temperature profile leads to substantially lower sound pressure levels (by 10 dB or more) than if a more reasonable temperature profile is included. Thus using a homogeneous temperature profile clearly is insufficient for making accurate predictions at en-route altitudes.

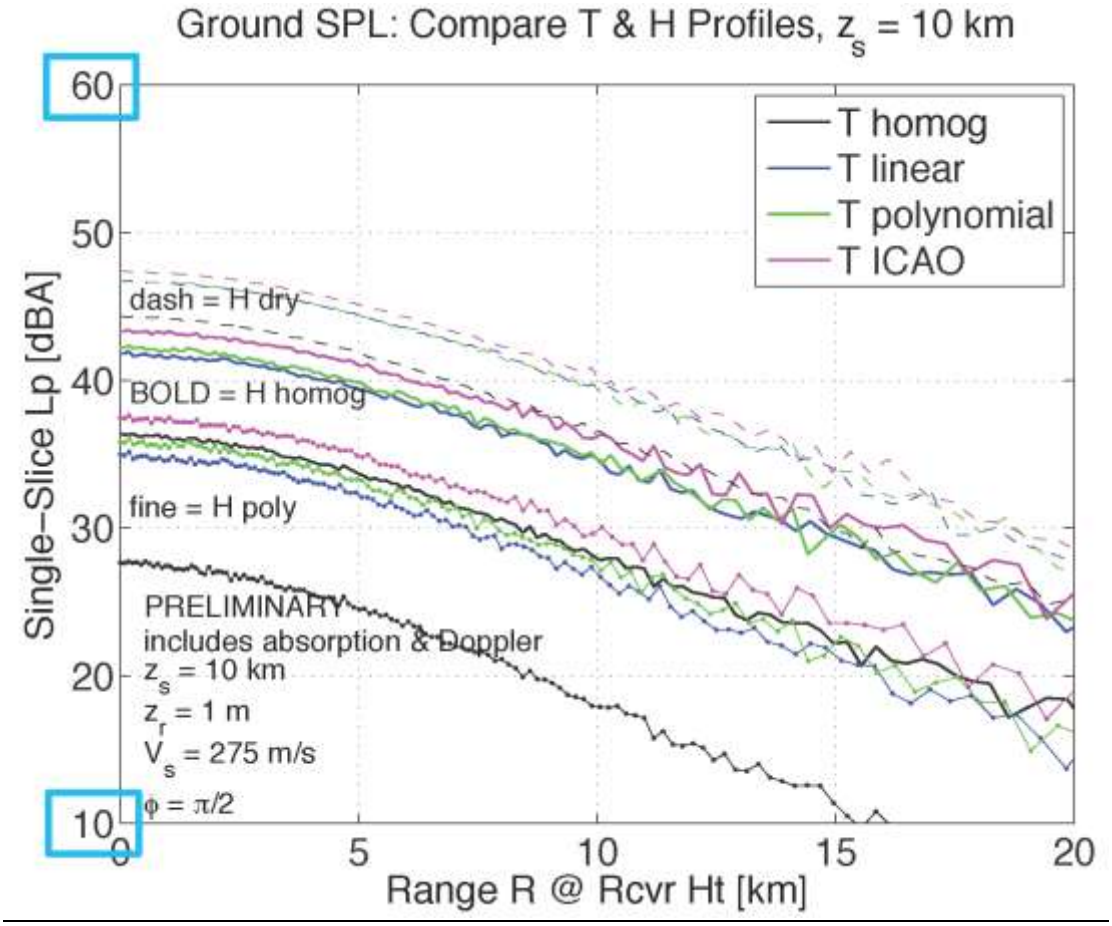

Fig. 5.6: Sound pressure levels on the ground for a single steady flight at 10 km altitude, comparing different temperature and humidity representations. See text for additional details. The dashed lines show the dry air predictions yield unrealistically high levels, but the homogeneous temperature profile (using surface temperature values for all heights) gives fairly low levels for this scenario.

Milestone(s)
N/A

Major Accomplishments
The project team now recommends that specific humidity be implemented in all noise propagation models instead of relative humidity.

Publications
None.

Outreach Efforts
Presentation by Graduate Research Assistant Rachel Romond at 16 August 2016 FAA External Tools teleconference.

Awards
None.

Student Involvement
Graduate Research Assistant Rachel Romond has been the primary person working on this task. She is working toward a Spring 2017 or Summer 2017 graduation with her Ph.D. in Acoustics.

Plans for Next Period
In the next year R. Romond will finish her Ph.D. dissertation, leading to scholarly publications.

References

- Wilson, D.K., Ostashev, V.E. and Mungiole, M. (2004). "Categorization schemes for near-ground sound propagation," in *Proceedings of the International Congress on Acoustics*, Kyoto, Japan, pp. 361-364.
- Saha, S., et al. (2010), NCEP Climate Forecast System Reanalysis (CFSR) 6-hourly Products, January 1979 to December 2010, http://dx.doi.org/10.5065/D69K487J, Research Data Archive at the National Center for Atmospheric Research, Computational and Information Systems Laboratory, Boulder, CO. Accessed 27 Mar 2015
- NASA Global Modeling and Assimilation Office (2012). *File Specification for MERRA Products*. GMAO Office Note No. 1, Version 2.3, NASA Goddard Space Flight Center, Greenbelt, MD.
- Salomons, E.M., van den Berg, F.H.A, and Brackenhoff, H.E.A. (1994). "Long-term average sound transfer through the atmosphere: predictions based on meteorological statistics and numerical computations of sound propagation," in *Proceedings of the 6th International Symposium on Long Range Sound Propagation*, Ottawa, Canada, pp. 209-228.
- Heimann, D. and Salomons, E.M. (2004). "Testing meteorological classifications for the prediction of long-term average sound levels," in Applied Acoustics **65**(10), pp. 925-950.
- Wyngaard, J.C. (2010). *Turbulence in the Atmosphere* (Cambridge University Press). ISBN 978-0-512-88769-4.
- International Civil Aviation Organization (1993) Manual of the ICAO Standard Atmosphere - extended to 80 kilometres (262 500 feet), Third Edition, ICAO Doc 7488/3.

Task 2 "Assess measurement data sets for noise propagation model validation"
The Pennsylvania State University

Objective(s)

Begin examination of aircraft measurement databases and ascertain their applicability for validating aircraft noise prediction tools.

Research Approach

This was the first year that the aircraft noise measurement databases became available for use in ASCENT noise projects. Specifically the DISCOVER-AQ Acoustics data became available from Volpe in January 2016, and it took several weeks for the Penn State team to learn how to use SQL to access that data, and even longer to be able to access the data in AEDT 2b. In addition the Vancouver Airport Authority data became available in June 2016, near the end of the project period for this task. Nonetheless, this data made it possible for the Penn State team to gain valuable experience with these datasets.

For example Figure 5.7 shows a simple comparison between DISCOVER-AQ Acoustics event number 35 and straight line propagation with spherical spreading. The upper flowchart shows the simple propagation procedure used. The left plot shows a top-down view of the flight track for event 35 with the microphone SP1 clearly denoted. The right plot shows the difference between the calculated and measured sound pressure levels as a function of aircraft distance from the microphone SP1. The differences between measurement and prediction are surprisingly small over most, but not all, of the flight path. Going through this exercise was invaluable for Penn State Graduate Research Assistant Manasi Biwalkar who performed the work.

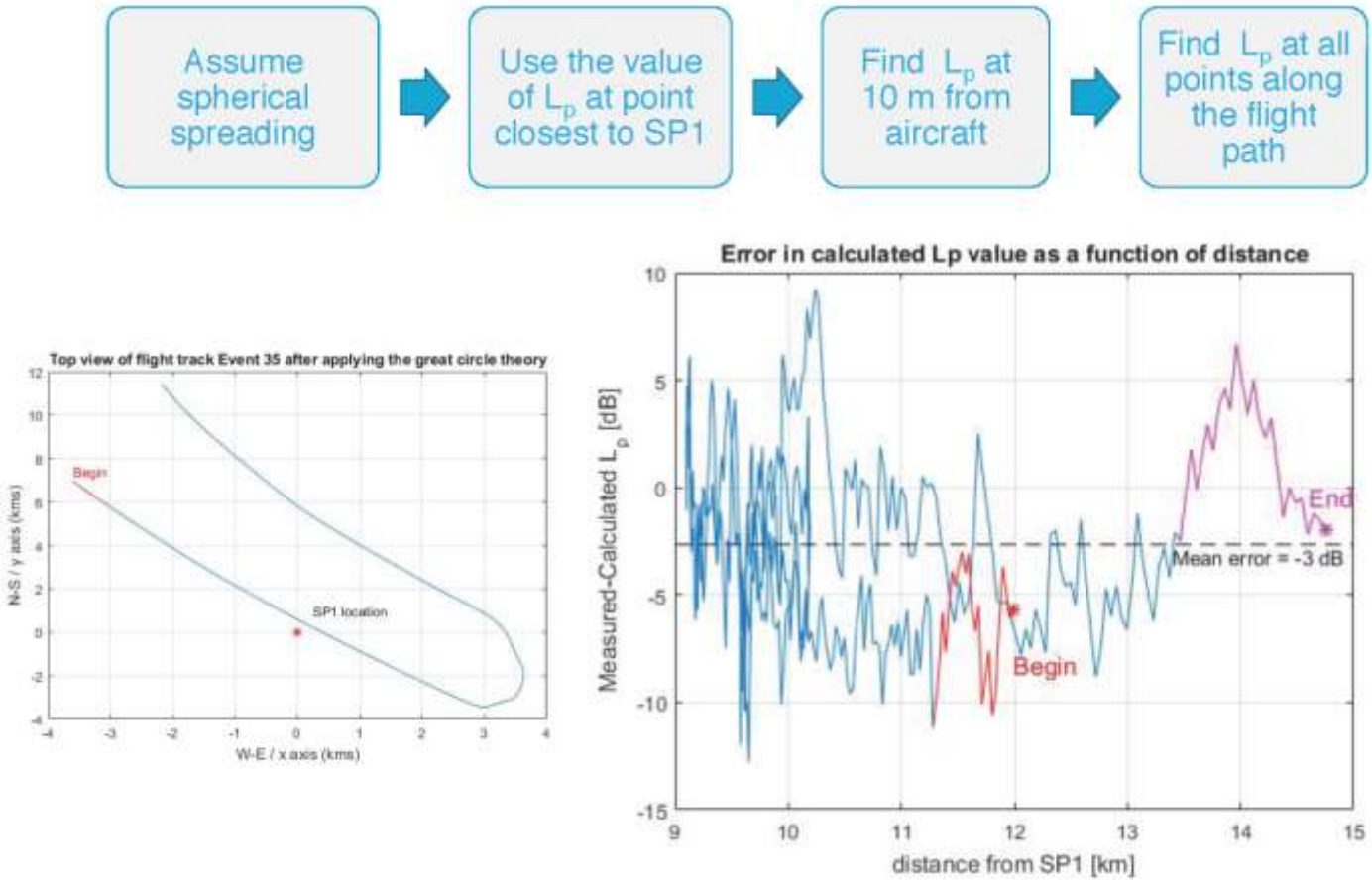

Fig. 5.7: Comparison between measured and predicted sound pressure levels on the ground for DISCOVER-AQ Acoustics Event 35. Top: method of calculation. Left: top down view of aircraft trajectory and microphone location. Right: differences in sound pressure level as a function of distance from the microphone.

Another parallel activity in this task was continued discussions with the European Aviation Safety Agency (EASA) regarding the possible use of the BANOERAC data set. Although drawn out over many months due to legal proceedings, the discussions went well, and that avenue will be discussed further in the annual report for ASCENT Project 40. ASCENT Project 5 was no-cost extended to December 31, 2017 to ensure that a Penn State subcontract to ANOTEC Engineering of Motril, Spain would remain in place. ANOTEC has agreed to provide flight trajectory data for BANOERAC via the subcontract, once the data sharing agreement with EASA is in place.

Milestone(s)
N/A

Major Accomplishments
Data from both DISCOVER-AQ Acoustics and the Vancouver Airport Authority were received by the Penn State Team and data analysis began.

Publications
None.

Outreach Efforts
None.

Awards
None.

Student Involvement
Graduate Research Assistant Manasi Biwalkar was the primary person working on this task. She continues working on her M.S. degree in the Penn State Graduate Program in Acoustics.

Plans for Next Period
Continue the assessment of the noise measurement data sets in ASCENT Project 40.

References
E. Boeker, *et al.*, "Discover-AQ Acoustics Measurement and Data Report," DOT-VNTSC-FAA-15-09 (2015).
M. Cheng, *et al.,* Vancouver Airport Authority [Private Communication] (2016).
BANOERAC Project final report, Document ID PA074-5-0, ANOTEC Consulting S.L. (2009).

Task 3 "Investigate the convective amplification effects of fast moving sources"
Purdue University

Aircraft noise has been a concern for districts near airports and sometimes for noise sensitive areas away from airports such as regions in the vicinity of national parks. To better understand the aircraft noise, an accurate numerical model is needed to predict its impact on neighborhood communities.

Most of the previous models for the sound fields above a locally reacting ground are based on the assumption that the source is stationary.[1] The ground admittance is therefore constant for a given source frequency.[1] Extending this solution to a moving source, Buret et al[2] (see also Ref. [1]) derived an asymptotic solution assuming that the acoustical properties of the ground surface is only dependent on the source frequency. However, the Doppler effect causes a frequency shift as the source moving past a stationary receiver. Indeed, the wavelength of the harmonic source appears to be ‘compressed’ for an approaching source. It becomes ‘stretched’ for a receding source. The well-known Doppler effect has a detrimental effect on the sound waves reflected from a locally reacting ground because its specific normalized admittance will be modified due to the source motion. Ignoring such effect will inevitably introduce a significant error in the prediction of the sound fields, especially for a source traveling at high speeds and locating at low elevations above the

ground surface. In a recent study, Ochmann[3] used a simplified ground model and derived an alternative solution for a point source moving above a flat ground with varying admittance. On the other hand, Dragna and Blanc-Benon[4] considered the sound fields due to a line source moving above a locally reacting ground. They obtained a two-dimensional asymptotic solution analogous to those given in Ref. [1, 2] but their solution provides a correct interpretation of the frequency-dependent ground model.

In this report, we endeavor to extend Dragna and Blanc-Benon's model to three-dimensions, i.e. we consider a point source moving above a locally reacting ground. The Lorentz transform converts the moving source problem into a 'standard' monopole located at a stationary point in the Lorentz frame. Section 2 addresses the formulation and the asymptotic analysis for the sound field due to a moving source. A brief discussion of the radial-slice fast field formulation (FFP) will also be presented. In Section 3, we present the numerical validation of the asymptotic formula and the FFP solution. Finally, conclusion is offered in Section 4.

2. Theoretical analysis

Consider a point monopole source of unit strength moving at a constant speed $c_0 M$ at a constant height $z = z_s$ in the positive x-direction where c_0 is the sound speed and M is the Mach number. Suppose that, at time $t = 0$, the source and receiver are situated, respectively, at $r_s = (0, 0, z_s)$ and $r = (x, y, z)$. Figure 1 shows the geometrical configuration of the problem. The ground is located at the $z = 0$ plane. A similar method based on Dragna and Blanc-Benon[4] is used to include the varying admittance in the theoretical analysis for the three-dimensional sound fields.

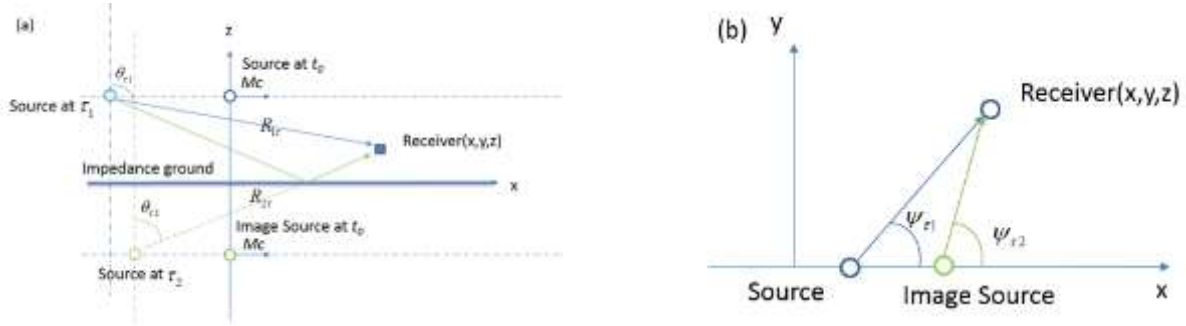

Figure 1: Schematic diagram to show the geometrical configuration of the problem with the source located at (0, 0, z_s) at $t = 0$. (a) Elevation, and (b) Plan view.

The governing wave equations for the source moving above a locally reacting plane is given by

$$\frac{\partial p}{\partial t} + \rho_0 c_0 \nabla \cdot \boldsymbol{u} = \rho_0 c_0^2 \delta(x - c_0 M t)\delta(y)\delta(z - z_s)e^{-i\omega_0 t} \quad (1)$$

$$\rho_0 \frac{\partial \boldsymbol{u}}{\partial t} + \nabla p = 0 \quad (2)$$

where p is acoustic pressure, $\boldsymbol{u} = (u_x, u_y, u_z)$ is the particle velocity, ω_0 is the angular frequency of the sound source and ρ_0 is the air density. The boundary condition at the ground surface, i.e. at $z = 0$, is specified by

$$\rho_0 c v_z(x, y, z = 0, t) + \int_{-\infty}^{+\infty} b(u)\, p(x, y, z = 0, t - u)du = 0 \quad (3)$$

where the impulse response $b(t)$ is determined by

$$\beta(\omega) = \int_{-\infty}^{+\infty} b(t)e^{i\omega t}dt \quad (4)$$

with $\beta(\omega)$ as the specific normalized admittance of the locally reacting ground, $\omega = 2\pi f$ and f is the source frequency.

We find it more convenient to use an acoustic potential ϕ which is defined as $p = -\rho \partial\phi/\partial t$ and $\boldsymbol{u} = \nabla \cdot \phi$. Using ϕ in Eqs. (1) and (3), we can show that

$$\Delta\phi - \frac{1}{c^2}\frac{\partial^2\phi}{\partial t^2} = \delta(x - cMt)\delta(y)\delta(z - z_s)e^{-i\omega_0 t} \quad . \quad (5)$$

$$\rho c \frac{\partial}{\partial z}\phi(x, y, z = 0, t) + \int_{-\infty}^{+\infty} b(u)\frac{\partial}{\partial t}\phi(x, y, z = 0, t - u)du = 0 \quad . \quad (6)$$

Applying the standard Lorentz transform:

$$x_L = \gamma^2(x - Mct), \quad y_L = \gamma y, \quad z_L = \gamma z,$$
$$t_L = \gamma^2(t - Mx/c),$$
$$\gamma = \left(1 - M^2\right)^{-\frac{1}{2}} \quad (7)$$

and introducing a two-dimensional Fourier transform, the wave equation in Eq. (5) can be reduced to a one-dimensional Helmholtz equation:

$$\frac{d^2\hat{\phi}}{dz_L^{\,2}} + \left(k_0^{\,2} - k_x^{\,2} - k_y^{\,2}\right)\hat{\phi} = \gamma^2\delta(z_L - z_{Ls}) \quad , \quad (8)$$

where the subscript *L* denotes the variables in the Lorentz space, ϕ_L and $\hat{\phi}$ form the Fourier transform pair:

$$\phi_L(x_L, y_L, z_L) = \frac{1}{4\pi^2}\int_{-\infty}^{+\infty}\int_{-\infty}^{+\infty}\hat{\phi}\left(k_x, k_y, z_L\right)e^{ik_x x_L + ik_y y_L}dk_x dk_y \quad , \quad (9)$$

$$\hat{\phi}\left(k_x, k_y, z_L\right) = \int_{-\infty}^{+\infty}\int_{-\infty}^{+\infty}\phi_L(x_L, y_L, z_L)e^{-i\left(k_x x_L + k_y y_L\right)}dxdy \quad . \quad (10)$$

The impedance boundary condition, Eq. (6), becomes

$$\frac{d\hat{\phi}}{dz_L}(k_x, k_y, z_L = 0) + i(k_0 + k_x M)\gamma\beta[(\omega_0 + k_x cM)\gamma^2]\hat{\phi}(k_x, k_y, z_L = 0) = 0 \quad (11)$$

It is tedious but straightforward to show that the solution for the velocity potential has a rather simple form as

$$\hat{\phi} = \frac{\gamma^2}{2ik_z}\left[e^{ik_z|z_L - z_{Ls}|} + R(k_x)e^{ik_z(z_L + z_{Ls})}\right] \quad , \quad (12)$$

where

$$R(k_x) = \frac{k_z - U}{k_z + U} = 1 - \frac{2U}{k_z + U} \quad , \quad (13)$$

$$U = (k_0 + Mk_x)\gamma\beta[(\omega_0 + c_0 Mk_x)\gamma^2] \quad , \quad (14)$$

$$k_z = +\sqrt{k^2 - k_x^2 - k_y^2} \quad . \quad (15)$$

Substitution of Eq. (12) into (9), we can obtain an integral representation of ϕ which can further be split into three terms. The first two terms can be identified as the Sommerfeld integrals for the direct and the image wave contribution. Consequently, the velocity potential ϕ becomes

$$\phi(x_L, y_L, z_L) = -\gamma^2 \frac{e^{ik_0 R_{1L}}}{4\pi R_{1L}} - \gamma^2 \frac{e^{ik_0 R_{2L}}}{4\pi R_{2L}} + I_\phi \quad (16)$$

where R_{1L} and R_{2L} are the direct distances measured from the source and its image to the receiver in the Lorentz frame. The third term of Eq. (16) is often referred as the diffraction integral given by

$$I_\phi = -\frac{1}{2\pi^2} \int_{-\infty}^{+\infty} \int_{-\infty}^{+\infty} \frac{\gamma^2}{ik_z} \frac{k_0 U}{k_z + k_0 U} e^{ik_x x_L + ik_y y_L + ik_{zL}(z+z_s)} dk_x dk_y \quad (17)$$

Changing the variables from the rectangular domain to their respective spherical-polar forms [i.e. (k_x, k_y, k_z) → (k_0, μ, ψ) and (x_L, y_L, z_L) → (R_{2L}, θ_L, ψ_L)]:

$$\begin{cases} k_x = k_0 \sin\mu\cos\psi; & k_y = k_0 \sin\mu\sin\psi; & k_z = k_0 \cos\mu \end{cases}, \quad (18)$$

$$\begin{cases} x_L = r_L \cos\psi_L; & y_L = r_L \sin\psi_L; & z_L = R_{2L}\cos\theta_L \end{cases}, \quad (19)$$

making use of the identity: $r_L = R_{2L}\sin\theta_L$ and the integral expression for the Bessel function,[5] we can simplify the diffraction integral as follows:

$$I_\phi = \frac{i\gamma^2}{4\pi} \int_{-\pi/2+i\infty}^{\pi/2-i\infty} \frac{\gamma D_L \beta(\omega_L)\sin\mu}{\cos\mu + \gamma D_L \beta(\omega_L)} H_0^{(1)}(k_0 r_L \sin\mu) e^{-ik_0 r_L \sin\mu} e^{ik_0 R_{2L}\cos(\mu-\theta_L)} d\mu \quad (20)$$

where ω_L and D_L are the modified frequency and the Doppler factor in the Lorentz frame:

$$\omega_L = \gamma^2 D_L \omega_0, \quad (21)$$

$$D_L(\mu) = 1 + M\sin\mu\cos\psi_L. \quad (22)$$

Figure 1(a) and 1 (b) show the schematic diagram for the corresponding polar and azimuthal angles, θ_L and ψ_L.

The acoustic pressure for the diffraction wave term can then be expressed by using Eq. (11) and noting

$$p = -\rho_0 \frac{\partial\phi}{\partial t} = -\rho_0\gamma^2 \frac{\partial\phi}{\partial t_L} + \rho_0 c_0 M\gamma^2 \frac{\partial\phi}{\partial x_L}. \quad (23)$$

In the Lorentz frame, the diffraction integral can then be written as

$$I_p = \frac{-\rho_0\omega_0\gamma^2}{4\pi} \int_{-\pi/2+i\infty}^{\pi/2-i\infty} \frac{\gamma D_L^2 \beta(\omega_L)\sin\mu}{\cos\mu + \gamma D_L \beta(\omega_L)} H_0^{(1)}(k_0 r \sin\mu) e^{ik_0 R_{2L}\cos\mu\cos\theta_L} d\mu \quad (24)$$

where the integration path starts at $-\pi/2 + i\infty$, moves through the points $-\pi/2$, $\pi/2$ and ending at $\pi/2 - i\infty$. In the special case of $M \to 0$ and $\gamma^2 \to 1$, the specific admittance of the ground surface is only dependent on the source frequency ω_0 which remains constant throughout the integration path.

A modified Miki model[6] is used to calculate the acoustical properties of the ground surface in which the normalized admittance is calculated by

$$\begin{cases} \beta(\omega) = \beta_\infty \tanh(-ik_c l) \\ \beta_\infty(\omega_L) = 1\Big/\left[1 + 0.459\left(i\sigma/\rho_0\omega_L\right)^{0.632}\right] \\ c_0 k_c(\omega_L) = \omega_L\left[1 + 0.643\left(i\sigma/\rho_0\omega_L\right)^{0.632}\right] \end{cases} \quad (25)$$

where σ is the effective flow resistivity and l is the layer thickness of the ground surface.

There is a pole in the integrand of Eq. (24) which gives rise to the surface wave pole contribution. The pole location, μ_p say, is determined by solving a non-linear equation:

$$\cos\mu_p + \gamma\left[1 + M\sin\mu_p\cos\psi_L\right]\beta(\omega_L) = 0 \quad (26)$$

where $\beta(\omega_L)$ is calculated by Eq. (25). The equation can be solved by means of the Newton-Raphson method.[7] Only the pole lies near the integration path is of interest in our problem, and the other poles have negligible effect on the total sound fields.

The diffraction integral, Eq. (24), cannot be evaluated analytically to yield an exact solution. However, it can be approximated asymptotically by the method of steepest descent. The details for approximating Eq. (24) can be found elsewhere[7] and the details will not be repeated here for brevity.

To present the analytic results for validation, it is more expedient to cast the formula in the emission time geometry. Here, the Doppler factor in the emission time τ (also known as the retarded time) is denoted by $D(\theta_\tau, \psi_\tau)$ where θ_τ and ψ_τ are the corresponding polar and azimuthal angles in the retarded time τ. Since $D(\theta_\tau, \psi_\tau) = D_L(\theta_L, \psi_L)$, it is possible to show that

$$D(\theta_\tau, \psi_\tau) = \frac{1}{1 - M\sin\theta_\tau\cos\psi_\tau} = \gamma^2\left(1 + M\sin\theta_L\cos\psi_L\right) \quad (27)$$

We can then specify the Doppler factors for the direct and reflected wave term as $D_{1\tau} = D(\theta_{\tau 1}, \psi_{\tau 1})$ and $D_{2\tau} = D(\theta_{\tau 2}, \psi_{\tau 2})$ where the subscripts 1 and 2 signify the corresponding parameters for the direct and reflected waves.

Substitution of Eq. (6) into Eq. (23), application of the inverse Lorentz transformation, and manipulation of the resulting equation yield the acoustic pressure in the emission time geometry:

$$p = p_d + p_i + I_p \quad (28)$$

where

$$p_d = -i\rho_0\omega_0 D_{1t}^2\left[1 - \frac{iD_{1\tau}M}{k_0 R_{1\tau}}(M - \cos\psi_{1\tau}\sin\theta_{1\tau})\right]e^{-i\omega_0 t}e^{ik_0 R_{1\tau}} / 4\pi R_{1\tau}, \quad (29)$$

$$p_i = -i\rho_0\omega_0 D_{2\tau}^2\left[1 - \frac{iD_{2\tau}M}{k_0 R_{2\tau}}(M - \cos\psi_{2\tau}\sin\theta_{2\tau})\right]e^{-i\omega_0 t}e^{ik_0 R_{2\tau}} / 4\pi R_{2\tau}. \quad (30)$$

The diffraction integral, i.e. the 3rd term of Eq. (28), can be evaluated asymptotically to give

$$I_p = -i\rho_0\omega_0 D_{2\tau}^2 e^{-i\omega_0 t}[V_{\theta\tau} - 1 + C(1 - V_{\theta\tau})F(w_a)]\frac{e^{ik_0 R_{2\tau}}}{4\pi R_{2\tau}} \quad (31)$$

where

$$V_{\theta\tau} = \frac{\cos\theta_{2\tau} - \beta(\omega_0 D_{2\tau})}{\cos\theta_{2\tau} + \beta(\omega_0 D_{2\tau})}, \quad (32)$$

$$C = \frac{r_\beta}{r_w}\frac{\sin\mu_p}{\sin\mu_p - \left.\frac{d\beta}{d\mu}\right|_{\mu=\mu_p}}\frac{1}{\sqrt{\sin\theta_L\sin\mu_p}}\frac{1 + M\cos\psi_L\sin\mu_p}{1 + M\cos\psi_L\sin\theta_L}, \quad (33)$$

$$F(w_a) = 1 + i\sqrt{\pi} w_a e^{-w_a^2} \operatorname{erfc}(-iw_a), \quad (34)$$
$$w_a^2 = ikR_{2L}[1 - \cos(\mu_p - \theta_L)],$$

with μ_p as the solution of Eq. (26). The function $F(w_a)$ is often referred as the boundary loss factor and w_a is termed as the numerical distance. In a recent work,[8] C in Eq. (31) is approximated as 1. In the current study, a more accurate value for C is given in Eq. (33) where

$$r_\beta = -\cos\mu_p / [\gamma(1 + M\sin\theta_L \cos\psi_L)\beta(D_{2\tau}\omega_0)], \quad (35)$$

$$r_\omega = w_a / w_\theta, \quad (36)$$

and

$$\omega_\theta = \sqrt{ik_0 R_{2\tau} D_{2\tau}/2}\left[\cos\theta_{2\tau} + \beta(\omega_0 D_{2\tau})\right]. \quad (37)$$

Substitution Eqs. (29), (30) and (31) into (28) and rearrangement of terms yield an analytical formula for the acoustic pressure of a moving source:

$$p = -i\rho_0\omega_0 e^{-i\omega_0 t}\left\{\Gamma_1 e^{ik_0 R_{1\tau}}/4\pi R_{1\tau} + \Gamma_2\left[V_{\theta\tau} - 1 + C(1 - V_{\theta\tau})F(w_a)\right]e^{ik_0 R_{2\tau}}/4\pi R_{2\tau}\right\} \quad (38)$$

where Γ_i (i = 1, 2) is the convective source strength of the direct and reflected wave terms given by,

$$\Gamma_i = D_{i\tau}^2\left[1 - \frac{iD_{i\tau}M}{k_0 R_{i\tau}}(M - \cos\psi_{i\tau}\sin\theta_{i\tau})\right]. \quad (39)$$

For an en-route aircraft, the boundary loss factor $F(w_a)$ is negligibly small. Furthermore, the second term in the convective source strength is small compared with the first term. Hence, the acoustic pressure above a locally-reacting ground may be simplified

$$p = \left(-i\rho_0\omega_0 e^{-i\omega_0 t}/4\pi\right)\left[D_{1\tau}^2 e^{ik_0 R_{1\tau}}/R_{1\tau} + V_{\theta\tau} D_{2\tau}^2 e^{ik_0 R_{2\tau}}/R_{2\tau}\right]. \quad (40)$$

Equations (39) and (40) are the main results of the current study. They provide an extension to allow predictions of sound fields due to a moving point source.

To validate the asymptotic formulas, a radial-slice fast field program (FFP) has been developed which follows Wilson's formulation.[9] In his study, Wilson calculated an approximate numerical solution for the three-dimensional sound fields due to a moving point source. In particular, we apply the polar representation of the wave equation in the FFP.[10] The integration over the azimuthal angle is carried out by an asymptotic method. The computation in the azimuthal direction is then collapsed into an evaluation at a single angle corresponding to the direct line of sight between the source and receiver. Thus, the time-consuming two-dimensional integral can be reduced to a simpler one-dimensional integral. Using this radial-slice approach, we can obtain accurate numerical solutions for validating Eq. (38).

3. Result and comparison

In presenting the numerical results, we shall use Transmission Loss (TL) which is defined by

$$TL = 20\log_{10}\left|\frac{p}{\rho\omega_0/4\pi}\right|. \quad (41)$$

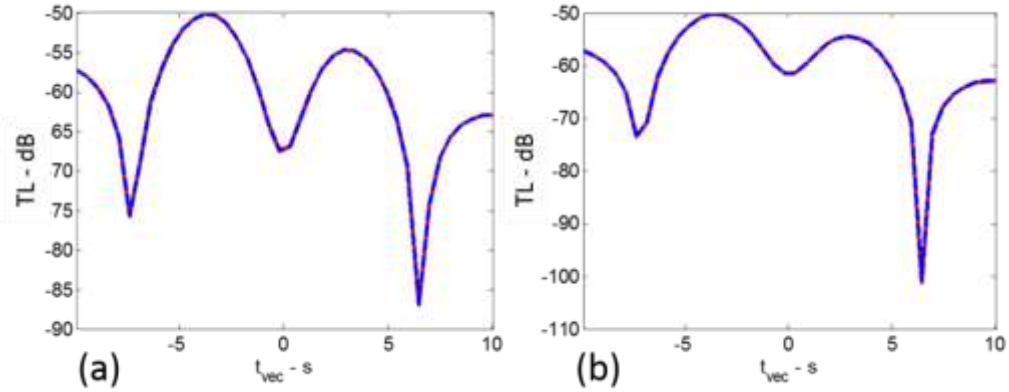

Figure 2: Asymptotic solution, Eq. (38) compare with the radial-slice FFP formulation. Blue line: FFP; Red dashed line: asymptotic solution, Eq. (38). The Miki one parameter model for hard-backed ground is used with the effective flow resistivity of 100 kPa sm^{-2} and a layer thickness of 0.01; The source, which has frequency of 300 Hz, moves with constant Mach number of 0.5 at height of 1000 m. The receiver is located at 1.2 m. The source passes through (0, *y,* 100) at t =0 with the off-set distance (a) y = 10 m; (b) y = 200 m.

It is the total sound field normalized with the free field sound pressure at 1 m from an equivalent stationary source. The Miki hard-back layered model is used to calculate the admittance of the ground surface. The parametric values of the effective flow resistivity (σ) of 100 kPa s m^{-2} and a layer thickness of 0.01 m are used in all numerical simulations presented in this paper. Figure 2(a), 2(b) and 3 show good agreements between the asymptotic solution, Eq. (38), and the radial-slice FFP solutions. In these plots, the source and receiver are located at 1000 m and 1.2 m respectively. The source moves with a Mach number of 0.5 and. The receiver is located at an offset distance of 10 m and 200 m for Fig. 2(a) and 2(b) respectively. On the other hand, the offset distance is set at y = 0 in Fig. 3, i.e. an overhead flight where the source is located directly above the receiver at t = 0. We see that these two prediction schemes agree in the majority of the time steps for $|t| > 0$ but the FFP results show significant fluctuations for the region near t = 0. Due to the assumption used, the FFP formulation cannot give accurate solutions at short horizontal range r in the region near t = 0. This numerical problem can be overcome by using a direct numerical integration scheme at the expense of longer computation times for each time step. We shall illustrate the accuracy in the use of the direct integration scheme in the following numerical simulations.

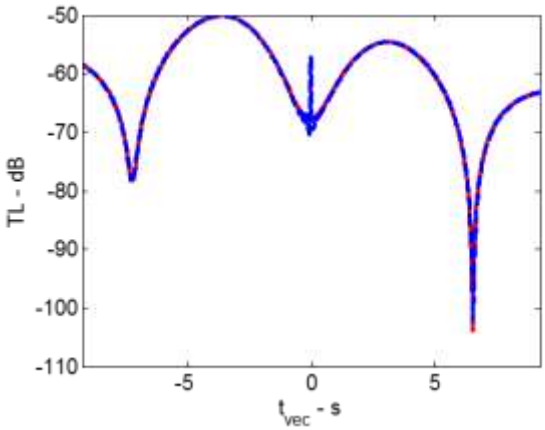

Figure 3: Asymptotic solution compare with radial-slice FFP formulation. Blue line: FFP solution; red dashed line: asymptotic solution. The same ground surface and geometry as Fig 1 are used except the offset distance, y = 0.

An assumption is often made on the admittance of the ground surface: it is evaluated at the source frequency which is kept constant for different time steps.[1,2] However, the well-known Doppler effect has caused a frequency shift for the moving source. In fact, the source frequency appears to be higher for an approaching source and this apparent frequency is lower when the source recedes. As a result, the apparent admittance of the ground surface varies at different time steps for the source traversing past the receiver. This assumption leads to two approximations in the asymptotic formula. First, the pole location, μ_p, has been approximated by reducing Eq. (26) to

$$\cos\mu_p + \gamma^2\left[1 + M\sin\mu_p\cos\psi_L\right]\beta(\omega_0) = 0 \quad (42)$$

Secondly, the factor C in Eq. (33) has been simplified to

$$C = \frac{r_\beta}{r_w}\frac{1}{\sqrt{\sin\theta_L\sin\mu_p}}\frac{1 + M\cos\psi_L\sin\mu_p}{1 + M\cos\psi_L\sin\theta_L}, \quad (43)$$

because $\partial\beta/\partial\mu = 0$ as $\beta(\omega_0)$ is constant. These two approximations in Eq. (38) can lead to significant errors in calculating the diffraction integrals especially for the situations with high source speeds and low source heights.

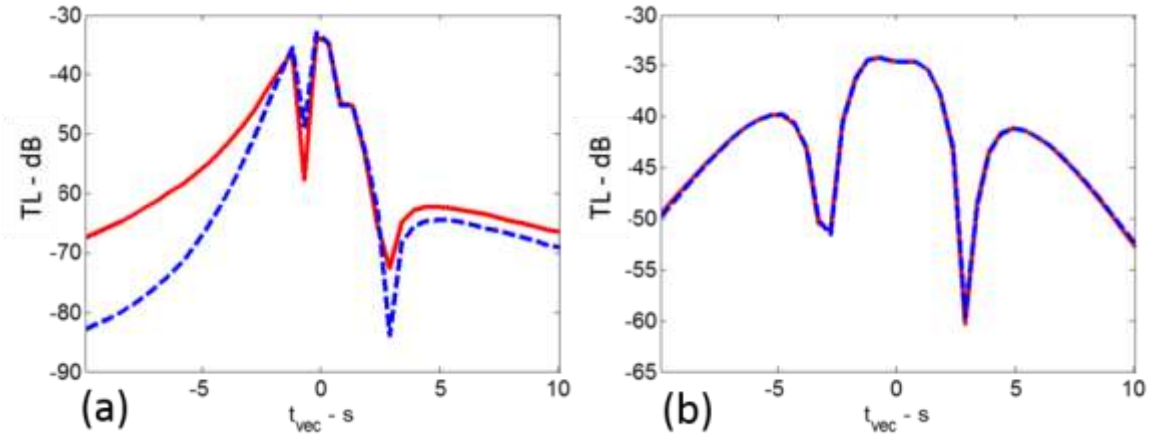

Figure 4: Comparison of asymptotic solutions for the model with a frequency-dependent admittance and a constant admittance at the source frequency. Red line: frequency-dependent model; Blue dashed line: constant admittance model. The same geometry, source frequency, and ground parameters as Fig. 3 are used but the Mach number is (a) M = 0.5, and (b) M = 0.1.

To illustrate the impact of ignoring the Doppler effect on the apparent ground admittance, we display in Fig. 4 the numerical results by using Eqs. (42) and (43) [instead of Eqs. (26) and (33)] in Eq. (38). In these two plots, the source has Mach numbers of 0.5 and 0.1 respectively. All other parameters are the same as Fig. 3. As shown in Fig. 4a (the left plot), there are significant errors in predicting the acoustic pressure especially when the source is located at longer ranges. On the other hand, the Doppler effect on the apparent admittance is insignificant if the source speed is low which is shown in Fig. 4b (the right plot) with the Mach number of 0.1.

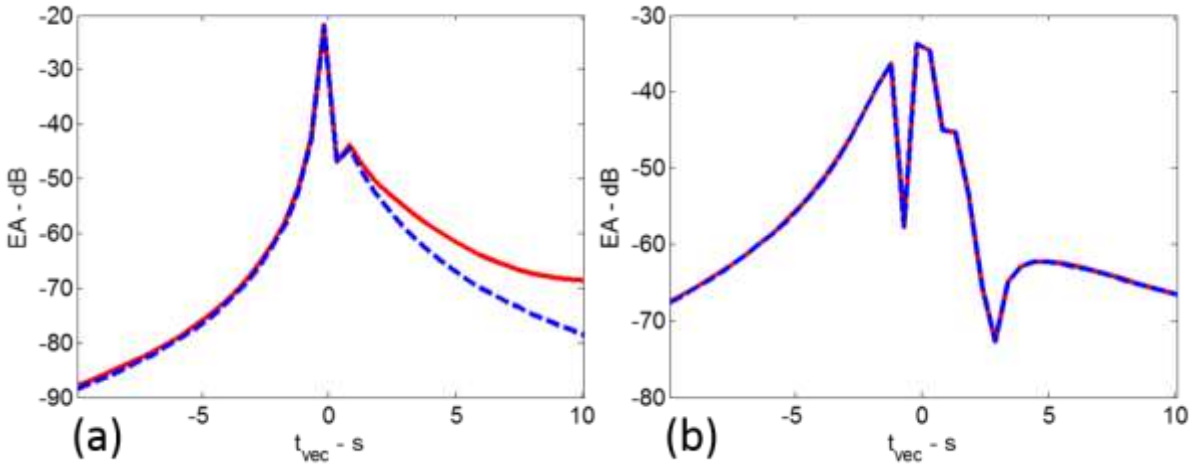

Figure 5: The importance of the ground wave term. Red line: direct integration scheme; Blue dashed line: asymptotic solution without the ground wave term, Eq. (40). Solid: asymptotic solution. The ground admittance and source frequency are the same as Fig. 2. The receiver is located (0, 0, 1.2) The source travels at constant Mach number of 0.5. The source is located at (a) z_s = 10 m, and (b) z_s = 100 m.

We end this section by showing significance of the ground wave term by comparing the numerical solution obtained by the direct numerical integration scheme with the results predicted by Eq. (40). The same ground admittance model and source frequency as Fig. 2 are used in the following numerical simulations. The receiver is located at (0, 0, 1.2) m. The source travels at a constant speed at a Mach number of 0.5. Two numerical simulations are presented in Fig. 5 with source height at 10 m and 100 m. It can be seen that when the source is close to the ground, the ground wave term becomes important when the receiver is located at a long distance from the moving source, i.e. near-grazing propagation. In addition, there is no numerical instability for the direct numerical scheme (near the region of t = 0) as compared with the FFP solution shown in Fig. 3.

4. Conclusion

A three-dimensional asymptotic formula for predicting the sound fields due to a source traveling at a constant speed above a locally reactive ground has been derived. Due to the Doppler effect, a frequency-dependent admittance model is required in order to give accurate numerical solutions. To validate the asymptotic formula, a three-dimensional radial-slice Fast Field Program (FFP) has also been implemented. Good agreements between the FFP solution and the asymptotic formula have confirmed the validity of these numerical solutions. Numerical simulations are also provided to investigate the validity of using various approximations[1,2] in earlier studies. Future work include the derivation of an asymptotic formula for the sound field caused by a source moving at a constant speed above a non-locally reacting ground.

Milestone(s)

N/A

Major Accomplishments

The project team now recommends that specific humidity be implemented in all noise propagation models instead of relative humidity.

Publications

None.

Outreach Efforts

Presentation by Graduate Research Assistant Yiming Wang at Noise Con 2016 at Providence RI.

Awards

N/A

Student Involvement

Graduate Research Assistant Bao Tong has been the primary person working on this task. Bao completed his PhD thesis in August 2015. Yiming Wang, who has just his preliminary exam, is currently a PhD student at Purdue. He has been working on this project since Summer 2015. A Master student Robert St. Claire spent the summer (work for a 6-credit self-study course) to work on the use of AEDT.

Plans for Next Period

Yiming Wang will aim to complete his preliminary within the next 2 years and aim to finish his Ph.D. dissertation in 2018. On the process of the research work, we aim to submit scholarly publications in refereed journals.

REFERENCES

K. Attenborough, K. M. Li, and K. Horoshenkov (2007). *Predicting outdoor sound*. Taylor & Francis, London and New York.
M. Buret, K. M. Li, and K. Attenborough (2006). "Optimizing of ground attenuation for moving sources," Applied Acoustics **67**, 135-156.
M. Ochmann (2013) "Exact solutions for sound radiation from a moving monopole above an impedance plane." The Journal of the Acoustical Society of America 133.4: 1911-1921.
D. Dragna and P. Blanc-Benon (2015). "Sound radiation by a moving line source above an impedance plane with frequency-dependent properties," Journal of Sound and Vibration **349**, 259-275.
M. Abramowitz and I. A. Stegun (1970). *Handbook of mathematical functions: with formulas, graphs, and mathematical tables*. 9th Ed. Dover Publication Inc., New York.
T. Komatsu (2008). "Improvement of the Delany-Bazley and Miki models for fibrous sound-absorbing materials," The Journal of the Acoustical Society of Japan **29**, 121-129.
K. M. Li and H. Tao (2014). "Heuristic approximations for sound fields produced by spherical waves incident on locally and non-locally reacting planar surfaces," The Journal of the Acoustical Society of America **135**, 58-66.
B. N. Tong and K. M. Li (2014). "Atmospheric effects on noise propagation from an en-route aircraft," In INTER-NOISE and NOISE-CON Congress and Conference Proceedings (Vol. 248, No. 1, pp. 656-663). Institute of Noise Control Engineering.
D. K. Wilson (1993). "Sound field computations in a stratified, moving medium," The Journal of the Acoustical Society of America **94**, 400-407.
B. N. Tong (2015). *Prediction and reduction of aircraft noise in outdoor environments*, PhD Thesis, School of Mechanical Engineering, Purdue University.